Chemical Science

ROYAL SOCIETY OF CHEMISTRY

EDGE ARTICLE

View Article Online
View Journal

Cite this: DOI: 10.1039/d6sc00989a

All publication charges for this article have been paid for by the Royal Society of Chemistry

Supramolecular assembly strategy of multinuclear platinum(II) complexes for proof-of-concept detection and extraction of perfluorohexanoic acid

Nicholas Chun-Ming Yeung,†[a] Zhen Chen,†[b] Ziyong Chen,[a] Eric Ka-Ho Wong[a] and Vivian Wing-Wah Yam *[a]

Wide applications of per-/poly-fluoroalkyl substances (PFASs) in manufacturing fluorinated-polymer coatings and products pose serious health and environmental threats due to their highly chemical robustness. The development of efficient sensors for detecting persistent organic pollutants is thus essential. In this study, we present the supramolecular assemblies of multinuclear platinum(II) complexes, which demonstrate the capability to detect and extract perfluorohexanoic acid (PFHxA) in deionized water. These platinum(II) complexes have exhibited remarkable photophysical properties and supramolecular self-assembly in mixed organic solvents, driven by Pt(II)···Pt(II) and π–π stacking interactions, to form two-dimensional supramolecular polymers with hexagonal and rectangular packing, manifested as sheet-like nanostructures. Specifically, the dynamic association of PFASs with the resulting nanosheets formed by platinum(II) complexes induces significant changes in the UV-vis absorption and emission spectra. Mechanistic studies, supported by molecular dynamics simulations, suggest that these pronounced spectroscopic changes are induced by the strong interactions of PFASs with platinum(II) complexes and the surrounding solvent molecules. By means of liquid-phase extraction, we have demonstrated the innovative use of platinum(II) supramolecular polymer networks for proof-of-concept detection and extraction of PFHxA in deionized water. This work provides important insights into the fundamental molecular design principles that are crucial for the future development of novel supramolecular functional materials.

Received 4th February 2026
Accepted 7th May 2026

DOI: 10.1039/d6sc00989a

rsc.li/chemical-science

Introduction

Per-/poly-fluoroalkyl substances (PFASs), as a class of synthetic chemical compounds with multiple fluorine atoms attached to an alkyl chain,[1] have been extensively employed in industrial and consumer products for decades and remain in widespread use today.[2] However, the robustness of their carbon–fluorine (C–F) bonds renders them highly stable towards degradation processes such as hydrolysis, photolysis, and biodegradation, leading to extreme environmental persistence after disposal.[3] Some PFASs exhibit environmental half-lives exceeding 8 years.[4] Consequently, PFAS residues are now frequently detected in rainwater and drinking water sources worldwide,[5] and prolonged exposure to PFASs has been linked to various cancers, numerous disorders, and reduced immune function.[6] In response to these significant health concerns, the United States Environmental Protection Agency proposed a national drinking water regulation in 2024 to limit six PFASs, including perfluorooctanoic acid (PFOA) and perfluorooctane sulfonate (PFOS).[7] Concurrently, the European Union enacted legislation regulating perfluorohexanoic acid (PFHxA) and related substances across a broad range of products.[8] The implementation of these stringent regulations has intensified the demand for sensitive, precise, and cost-effective PFAS detection methods, driving considerable research efforts in this field. Recently, absorbance- and fluorescence-based spectral methods have attracted significant attention for PFAS detection, offering advantages such as low cost, rapid response, and user-friendliness. A diverse array of engineered sensors has been developed for this purpose, including those based on small molecules,[9–13] nanoparticles,[14] polymers,[15,16] metal clusters,[17] and metal–organic frameworks (MOFs).[18,19] The interaction between PFASs and these sensors typically induces colorimetric changes visible to the naked eye and/or detectable using smartphone-based platforms.

Platinum(II) complexes, characterized by their d^8 electronic configuration and square-planar geometry, exhibit a renowned propensity for forming metal–metal interactions.[20–24] These interactions underpin their intriguing spectroscopic and luminescence properties, as well as their distinct self-assembly behavior.[25–31] Within supramolecular chemistry, platinum(II) complexes serve as versatile building blocks for sophisticated

[a]Institute of Molecular Functional Materials, State Key Laboratory of Synthetic Chemistry and Department of Chemistry, The University of Hong Kong, Pokfulam Road, Hong Kong, P. R. China. E-mail: wwyam@hku.hk

[b]Institute of Materials Research, Tsinghua Shenzhen International Graduate School, Tsinghua University, Shenzhen 518055, P. R. China

† These authors contributed equally to this work.

nanostructures, utilizing Pt(II)···Pt(II), π–π stacking, and other noncovalent interactions. Guided by Pt(II)···Pt(II) and π–π stacking interactions, recent years have witnessed the self-assembly of diverse molecular architectures,[32–34] liquid crystals,[35] metallogels[36–39] and other well-defined nanostructures.[40–43] The versatility of platinum(II) complexes stems from the ability to fine-tune their properties through strategic ligand design, enabling tailoring for potential applications in fields such as resistive memory,[43–45] imaging[46–48] and material sciences.[49,50]

Recently, our group reported a honeycomb-like two-dimensional (2D) supramolecular polymer (SP) comprising Pt(II)···Pt(II) dimers formed by a trinuclear complex.[29] This SP could be processed into multifunctional separation membranes capable of capturing anionic Pt(II) species in water[29] and precisely sieving nanoparticles based on size.[30] Furthermore, this SP has been engineered into stimuli-responsive materials capable of modulating water permeability through pH changes.[31] In this work, we present a proof-of-concept supramolecular strategy for the detection and extraction of PFHxA. We found that PFHxA, acting as an acidic analyte, can perturb the self-assembly behaviors of the multinuclear platinum(II) complexes and induce significant spectral changes. By leveraging liquid-phase extraction, we have demonstrated the proof-of-concept detection and extraction of PFHxA in deionized water.

Results and discussion

Building on our previous work where a trinuclear platinum(II) complex—featuring three cationic alkynylplatinum(II) terpyridine units, each with six dodecyl side chains—served as a monomer for 2D SPs,[29] this study introduces novel multinuclear Pt(II) complexes, mesitylene-core trinuclear complex **1** and pyrene-core tetranuclear complex **2** (Scheme 1). We hypothesize that the hydrophobic effects from the dodecyl chains, synergistically with π–π and directional Pt(II)···Pt(II) interactions, will direct their supramolecular self-assembly into two-dimensional nanoarchitectures. The ligands of **1** and **2** were synthesized through copper(I)-catalyzed azide–alkyne cycloaddition (CuAAC) reactions[51] between alkyne-functionalized pyridine and 1-dodecyl azide, resulting in the formation of 2,6-bis(1,2,3-triazol-4-yl)-pyridine (btp). Subsequently, the btp moiety was attached to the mesitylene/pyrene core *via* Sonogashira coupling reactions.[52] Metal coordination reactions according to literature procedures[29,53] yielded the target complexes.

The dissolution of **1** and **2** in chloroform ($CHCl_3$) at 298 K at concentrations of 10^{-6} M results in pale yellow and red solution, respectively. The UV-vis absorption spectra (Table S1 and Fig. S1a) of both complexes feature high-energy absorption bands at 300–365 nm, which are assigned to the intraligand (IL) transitions [π → π*(btp)] of the btp ligands.[53,54] The lower energy absorption bands of **1**, observed within the range of 365–450 nm, are tentatively assigned to the spin-allowed intraligand charge transfer (ILCT) [π(mesitylene) → π*(btp)] transitions of the mesitylene-core ligand, with contributions from the spin-allowed metal-to-ligand charge transfer (MLCT) [dπ(Pt) → π*(btp)]. With a more extended π-conjugated system, the more red-shifted absorption bands of **2** at 422 nm and 455–600 nm are tentatively assigned to the spin-allowed MLCT[dπ(Pt) → π*(btp)] and the ILCT[π(pyrene) → π*(btp)] transitions, respectively. These assignments are further supported by DFT and TDDFT calculations (Fig. S2–S5 and Tables S2–S4). The vibronic emission bands (**1**, λ_{max} = 550 nm; **2**, λ_{max} = 565 nm) (Table S1 and Fig. S1b) with vibrational progression spacings of 1200–1400 cm^{-1} and lifetimes in the microsecond regime (**1**, τ = 0.3 μs; **2**, τ = 0.2 μs) are attributed to a ^{3}ILCT[π(mesitylene/pyrene) → π*(btp)] excited state origin. Interestingly, **2** demonstrates more sensitive concentration-dependent

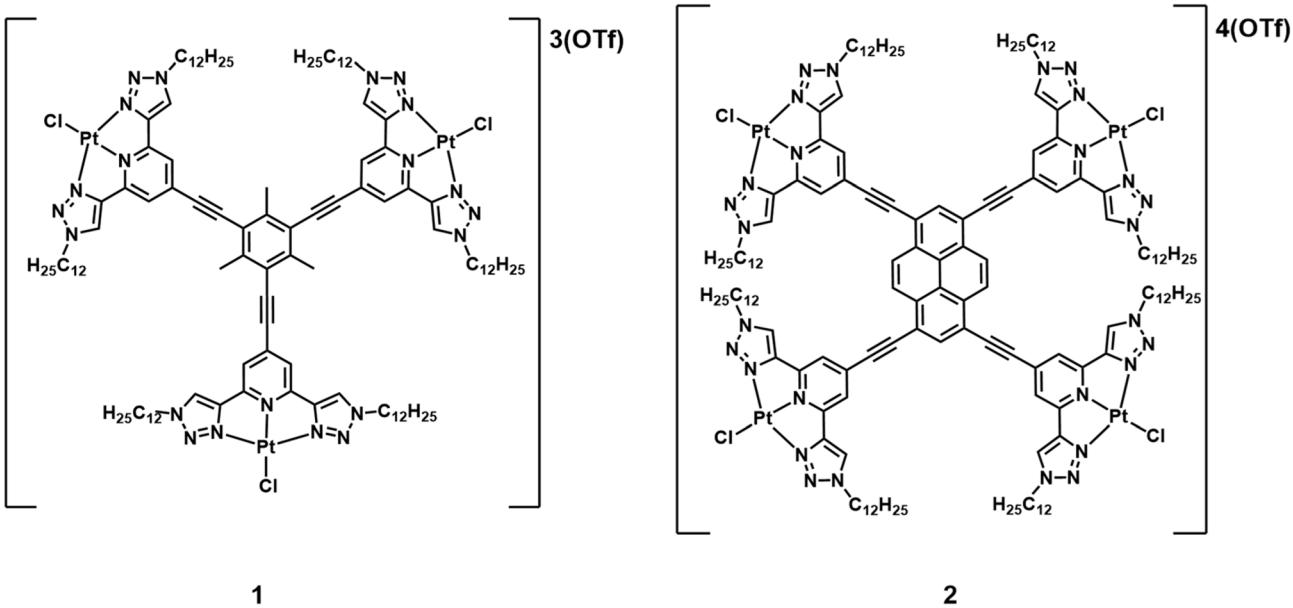

Scheme 1 Molecular structures of **1** and **2**.

emission spectral changes than **1**. As the concentration increases from 10^{-6} to 10^{-4} M, the vibronic emission band (λ_{em} = 565 nm) of **2** (Fig. S6c) undergoes a red shift and transforms into a structureless emission band (λ_{em} = 635 nm). This lower-energy emission may originate from self-assembled species, as evidenced by the larger aggregate sizes observed at higher concentrations in dynamic light scattering (DLS) experiments (Fig. S6d). The ^{1}H NMR spectra of **1** (Fig. S7) and **2** (Fig. S8) with concentrations of 10^{-4} M in $CDCl_3$ at ambient temperature display broadened aromatic signals. This phenomenon is particularly pronounced in **2**, where only the signals corresponding to the dodecyl side chains can be assigned. The observed line broadening phenomenon in ^{1}H NMR spectra, along with the concentration-dependent aggregate sizes and emission spectral changes, supports the presence of self-assembly processes in solutions, motivating more detailed investigation into their supramolecular self-assembly behaviors.

Our initial strategy to promote solution-state self-assembly involves mixing $CHCl_3$ solutions of the platinum(II) complexes with *n*-hexane, a poor solubilizing solvent for these complexes. The process is systematically monitored by UV-vis spectroscopy, emission spectroscopy and DLS experiments. As the proportion of *n*-hexane in the $CHCl_3$ solution increases, the absorbance of the spin-allowed IL, ILCT and MLCT transitions of both complexes decreases (Fig. 1a and b). Concurrently, larger aggregates are revealed in the DLS experiments (Fig. S9). The observed drop in absorbance in the IL, ILCT, and MLCT transitions, particularly in the case of **1**, can be attributed to the stacking of molecules in solution, resulting in hypochromism.[55] Notably, an absorption tail at *ca.* 610 nm emerges in the UV-vis absorption spectra of **2** (Fig. 1b). This lower-energy absorption band, which deviates from Beer's law (Fig. S10), is assigned to the spin-allowed metal–metal-to-ligand charge transfer (MMLCT) transition, arising from the formation of Pt(II)···Pt(II) interactions during supramolecular self-assembly. Corresponding emission studies (Fig. 1c and d) reveal photoluminescence (PL) changes upon increasing *n*-hexane content. The initial vibronic-structured ^{3}IL emission bands (**1**, λ_{em} = 550 nm; **2**, λ_{em} = 565 nm) have red-shifted and are accompanied by the gradual appearance of new emission bands (**1**, λ_{em} = 682 nm; **2**, λ_{em} = 618 nm). These lower-energy emission bands are ascribed to originate from the ^{3}MMLCT excited state of the aggregated platinum(II) complexes.

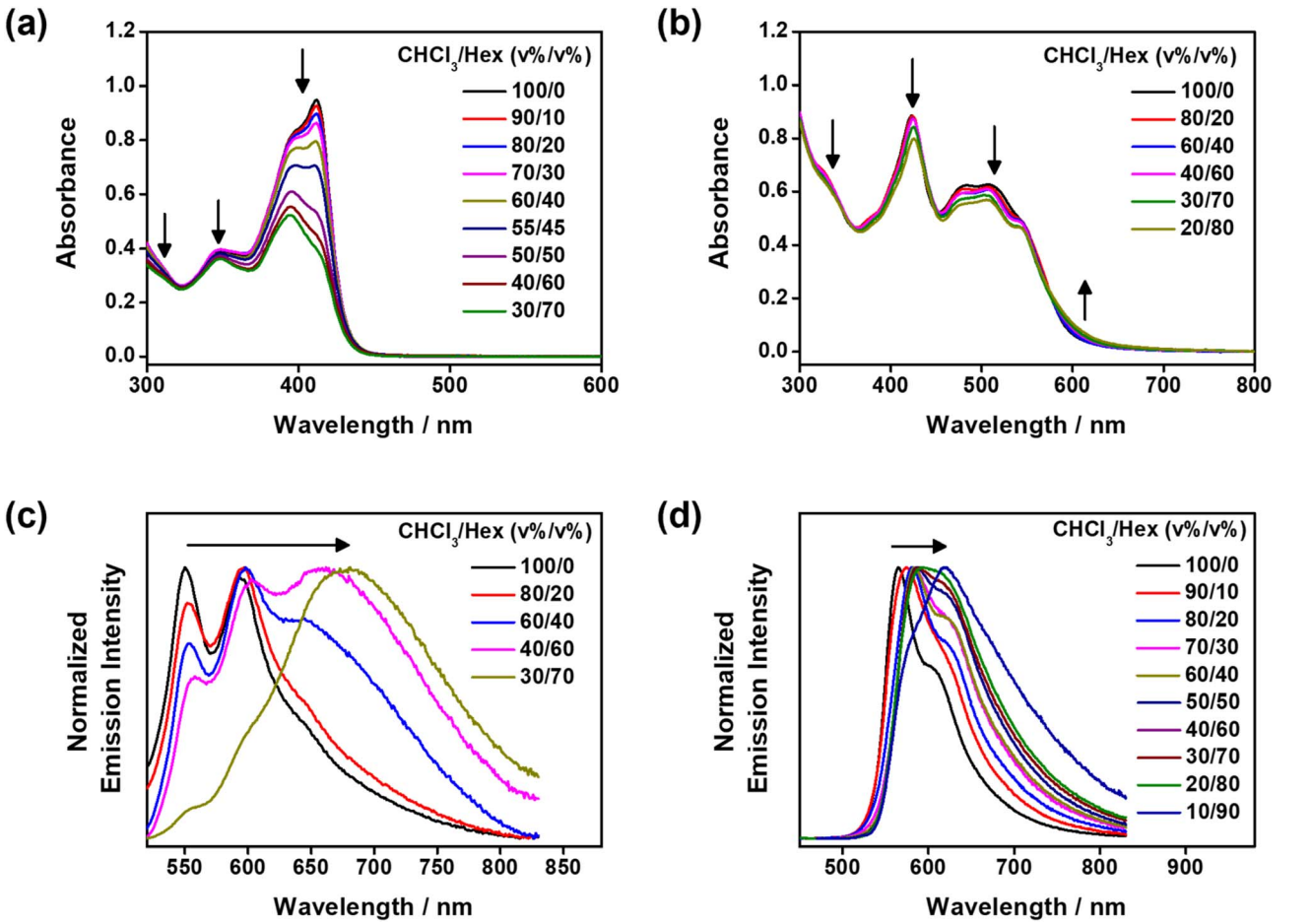

Fig. 1 UV-Vis absorption spectra of (a) **1** and (b) **2** upon increasing *n*-hexane content in $CHCl_3$ solution. Normalized emission spectra of (c) **1** and (d) **2** upon increasing *n*-hexane content in $CHCl_3$ solution.

Further structural characterization of the self-assembled materials has been conducted using microscopy and X-ray scattering techniques. Tapping-mode atomic force microscopy (AFM) images of drop-cast samples (Fig. 2a and b) reveal two-dimensional multi-layered nanosheets for both complexes, with average interlayer thicknesses of 6.41 nm for **1** and 4.24 nm for **2**. Similarly, scanning electron microscopy (SEM) (Fig. 2c and d) images confirm the formation of sheet-like aggregates. Wide-angle X-ray scattering (WAXS) analysis of a powdered sample of **1** at 298 K displays intense reflection peaks consistent with a simulated 2D hexagonal packing model (Fig. 2e). The peaks can be indexed to the (100), (200), ($3\bar{1}0$) and (220) planes of a 2D hexagonal lattice, revealing interplanar $\pi\cdots\pi$ and Pt$\cdots$Pt distances (Table S5). These results collectively indicate that **1** adopts a 2D SP with honeycomb-like nanostructures, exhibiting a cavity size of 4.01 nm derived from the *d*-spacing of the (100) plane (Fig. 2g). On the other hand, the WAXS pattern of **2** exhibits reflections consistent with a simulated 2D rectangular packing model (Fig. 2f). The peaks can be assigned to the (200), (020), and (220) planes of a 2D rectangular lattice (Table S6), which suggests that **2** self-assembles into a rhombic two-dimensional SP nanostructure (Fig. 2h). The corresponding lattice parameters, calculated from the *d*-spacings of the (200) and (020) planes, are 5.52 nm and 2.92 nm. Grazing-incidence X-ray diffraction (GI-XRD) analysis of the platinum(II) complexes drop-cast on silicon wafers (Fig. S11) reveals the absence of spot-like reflections, suggesting that the 2D SP nanosheets though highly ordered, lack long-range molecular orientation in thin-films.

Owing to the hydrophobicity imparted by dodecyl chains and the intrinsic cavities provided by the self-assembled nanostructures, we have explored the potential interactions between the platinum(II) complexes and PFASs. In initial investigations, equal concentrations of trifluoroacetic acid (TFA), perfluorobutanoic acid (PFBA) and PFHxA are separately introduced to 70% *n*-hexane-$CHCl_3$ solutions of **1** and **2**. For comparison, non-fluorinated carboxylic acid analogues, including acetic acid (AcOH), butyric acid (C_3H_7COOH), caproic acid ($C_5H_{11}COOH$), and other control compounds, including 1-bromoperfluorohexane ($C_6F_{13}Br$) and triethylamine (NEt_3), were examined. Upon the addition of PFASs, significant changes in both the absorption and emission spectra are observed (Fig. 3, S12 and S13), with PFHxA inducing the most notable effects. Specifically, PFASs trigger a drop in MMLCT absorption (λ_{max} = 543–660 nm) (Fig. 3b) of **2**, while simultaneously causing a drop in ^{3}MMLCT emission (λ_{max} = 618 nm) and a growth in ^{3}ILCT emission (λ_{max} = 554 nm) (Fig. 3c). The PL enhancement triggered by PFASs surpasses the responses induced by the non-fluorinated analogues or controls (Fig. 3c). As for **1**, the absorption bands at 400 nm are intensified (Fig. S13a) following the addition of PFASs, which is accompanied by a drop in ^{3}MMLCT emission (λ_{max} = 703 nm) and a growth in ^{3}ILCT emission (λ_{max} = 554 nm) (Fig. S13b).

A comprehensive titration study involving the platinum(II) complexes and the PFASs has been performed (Fig. S14–S18). The titration analysis of **1** with PFHxA (Fig. S14a and b) reveals a drop in the ^{3}MMLCT emission band at 703 nm and a growth of a vibronic-structured emission band at 554 nm. On the other hand, the titration study of **2** with PFHxA reveals concentration-dependent spectral evolution. A new emission band has emerged at 554 nm (Fig. 3e), gradually developing into a vibronic structure. Similar but attenuated changes have occurred with PFBA (Fig. S15 and S17) and TFA (Fig. S16 and S18). The magnitudes of absorbance changes (Fig. S19) and luminescence enhancement (Fig. S20) are found to correlate with PFAS acidity, which follows the trend PFHxA > PFBA ≈

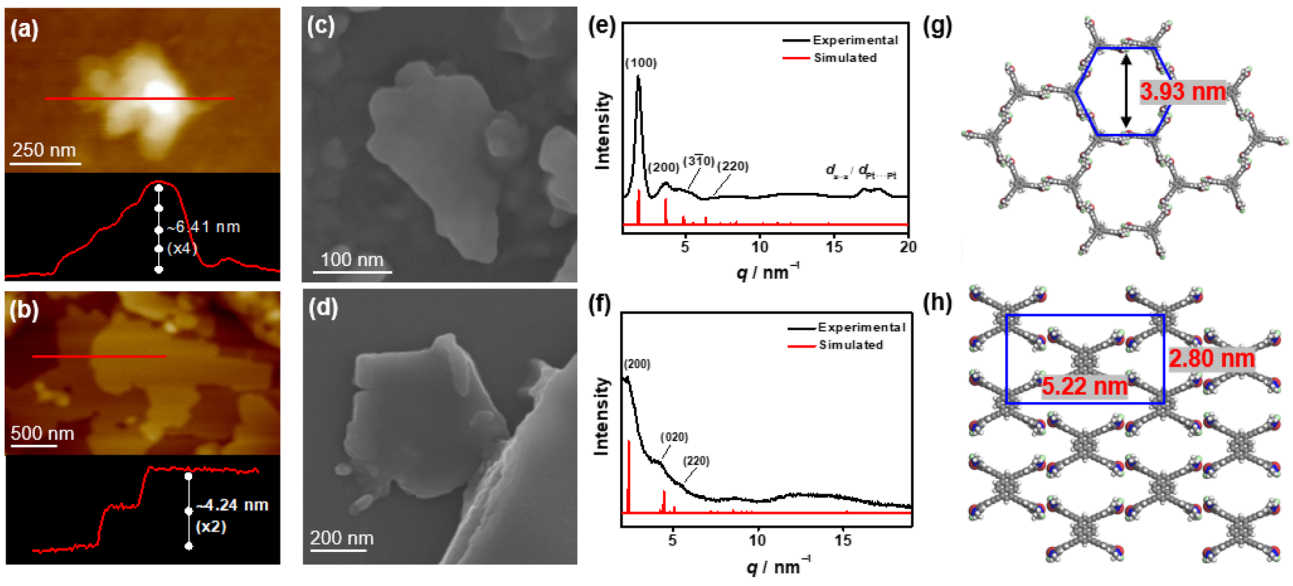

Fig. 2 Tapping-mode AFM images and height profiles of (a) **1** and (b) **2** prepared by drop-casting on silicon wafers. SEM images of (c) **1** and (d) **2** prepared by drop-casting on copper-carbon grids. Experimental and simulated WAXS patterns of (e) **1** and (f) **2** at 298 K. The simulated molecular packing model of (g) a 2D hexagonal lattice self-assembled from **1** and (h) a 2D rectangular lattice self-assembled from **2**.

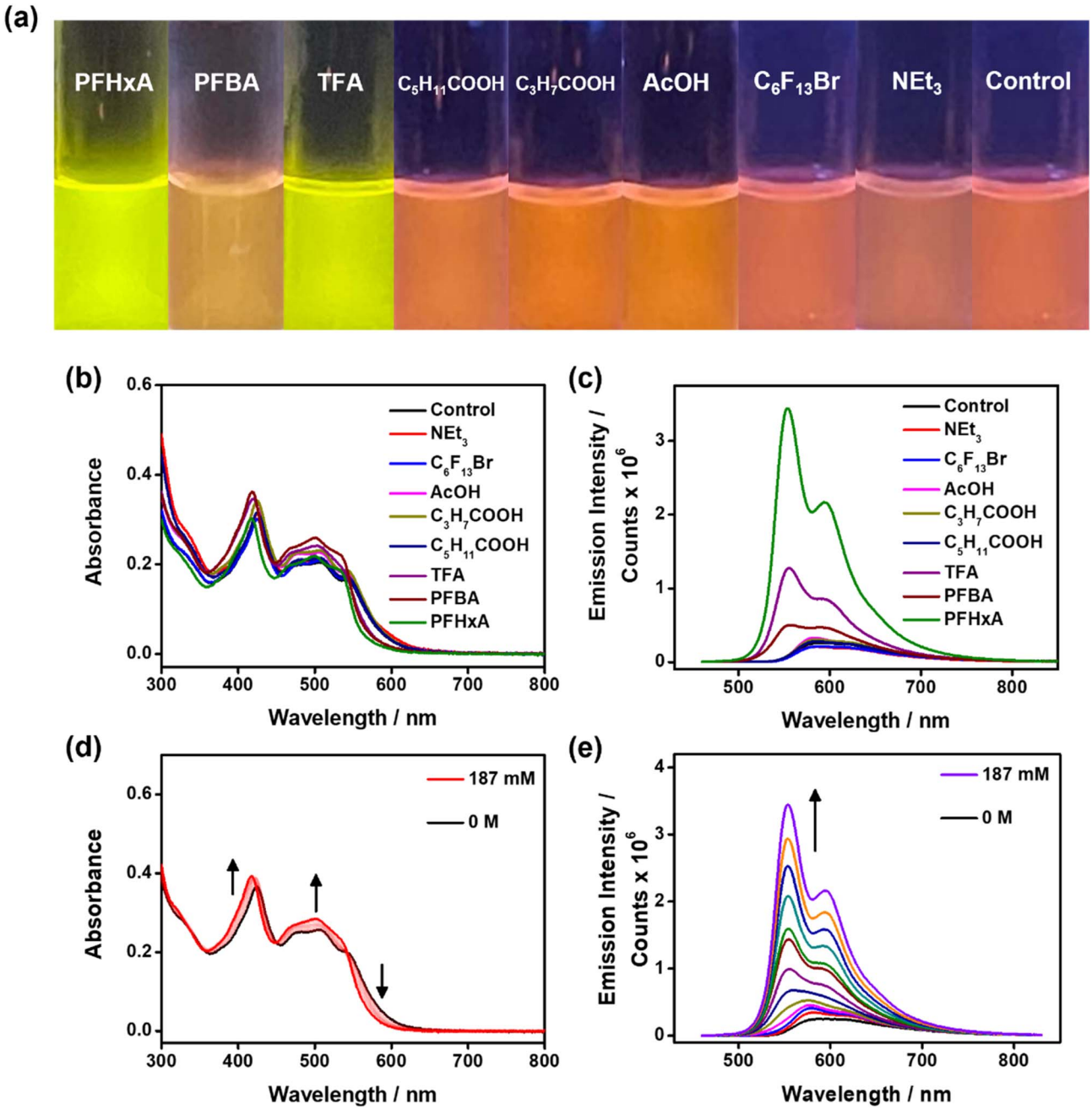

Fig. 3 (a) Photographs under a UV-light source (λ_{ex} = 365 nm), (b) UV-vis absorption spectra and (c) emission spectra of **2** (6.23 μM) in 70% *n*-hexane-$CHCl_3$ upon the addition of various chemicals (187 mM). (d) UV-Vis absorption and (e) emission spectral changes of **2** (6.23 μM) in 70% *n*-hexane-$CHCl_3$ upon incremental addition of PFHxA. The excitation wavelength is 425 nm.

TFA. Notably, the PFAS-induced vibronic emission bands resemble monomeric emissions of **1** and **2** in dilute $CHCl_3$ solution (Fig. S6). DLS analyses (Fig. S21) have shown smaller aggregates after the addition of PFASs, suggesting that the greenish-yellow emission bands of **1** (λ_{em} = 554 nm) and **2** (λ_{em} = 554 nm) are originated from monomeric ^{3}IL excited states of the platinum(II) complexes, implying that the PFAS triggers de-aggregation of self-assembled nanostructures. Critically, control experiments with non-fluorinated carboxylic acids (AcOH, C_3H_7COOH, and $C_5H_{11}COOH$) and non-acidic fluorocarbon ($C_6F_{13}Br$) show minimal spectral perturbations, confirming that both the acidic carboxylic group (–COOH) and perfluoroalkyl chain are essential for assembly disruption.

To investigate the aggregation behaviors of **1** and **2** in the presence of $C_5F_{11}COOH$ (PFHxA) and control compounds ($C_5H_{11}COOH$ and $C_6F_{13}Br$), atomistic molecular dynamics (MD) simulations[56–59] have been conducted on the mononuclear model complex cation **3** (Fig. S22). Our previously developed Lennard-Jones force field parameters for platinum [σ(Pt) = 0.33298 nm and ε(Pt) = 5.267 kJ mol^{-1}] have been adopted to describe Pt(II)···Pt(II) interactions within the aggregates.[60,61] Four solvent environments are examined for **3**, including the

70% *n*-hexane-$CHCl_3$ mixture and the solutions containing $C_5F_{11}COOH$, $C_5H_{11}COOH$, or $C_6F_{13}Br$ in 70% *n*-hexane-$CHCl_3$ (Table S7). In the 70% *n*-hexane-$CHCl_3$ mixture, the first peak of the radial distribution function (RDF) $g_{Pt-Pt}(r)$ at approximately $r = 0.39$ nm is prominent (Fig. 4a and Fig. S23), indicating a large extent of occurrence of extensive self-assembly of **3** driven by Pt(II)···Pt(II) and π–π stacking interactions. The addition of $C_5H_{11}COOH$ or $C_6F_{13}Br$ could not significantly disrupt

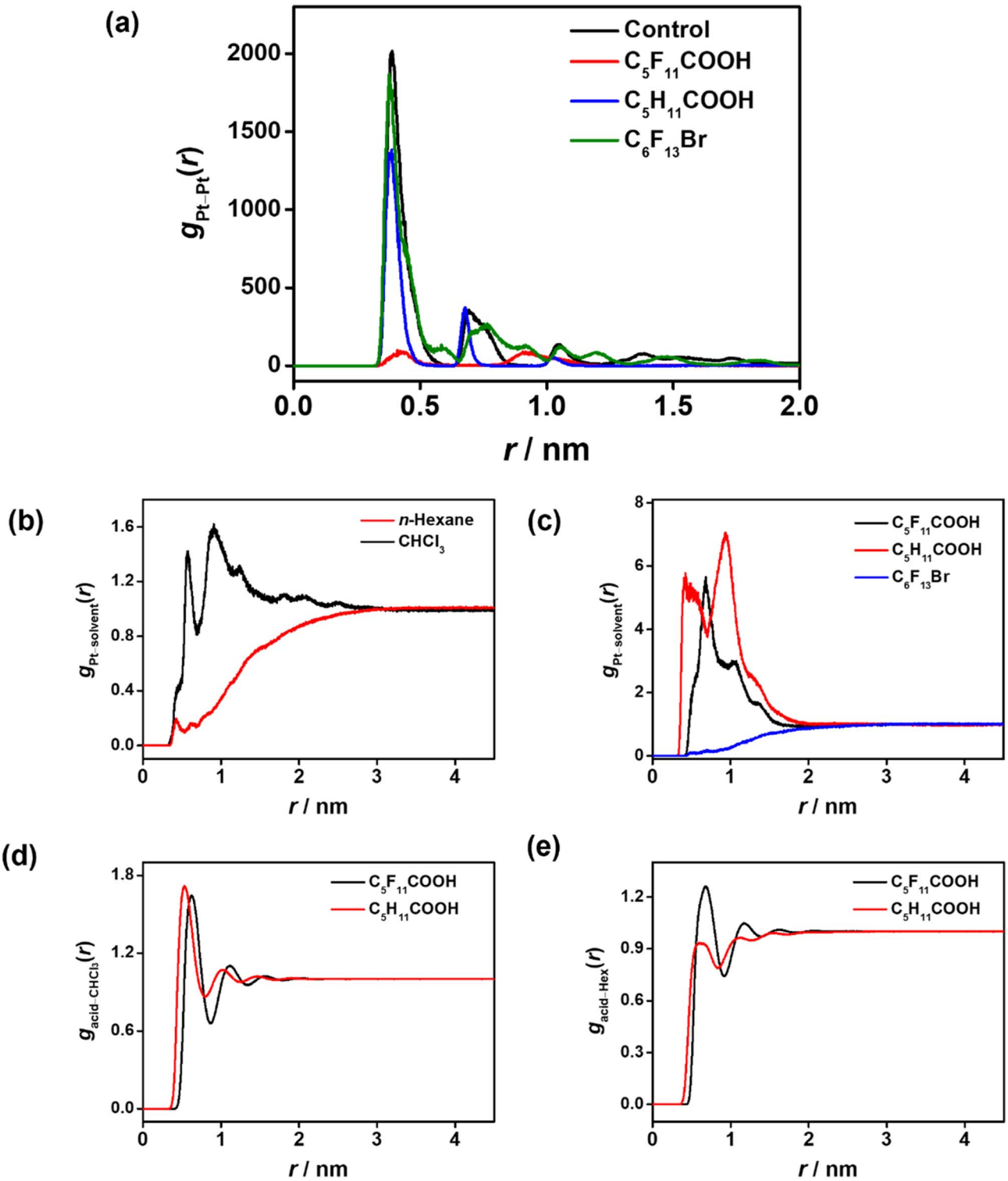

Fig. 4 (a) Radial distribution function $g_{Pt-Pt}(r)$ for the complex cation **3** in the presence of $C_5F_{11}COOH$, $C_5H_{11}COOH$ and $C_6F_{13}Br$. Radial distribution function $g_{Pt-solvent}(r)$ between **3** and (b) *n*-hexane and $CHCl_3$ and (c) $C_5F_{11}COOH$, $C_5H_{11}COOH$ and $C_6F_{13}Br$. Radial distribution function $g_{acid-solvent}(r)$ between $C_5F_{11}COOH$/$C_5H_{11}COOH$ and (d) $CHCl_3$ and (e) *n*-hexane.

aggregation, as evidenced by comparable $g_{Pt-Pt}(r)$ peak heights. However, the presence of $C_5F_{11}COOH$ results in a substantial reduction in the first $g_{Pt-Pt}(r)$ peak intensity, suggesting that $C_5F_{11}COOH$ effectively inhibits the aggregation of **3**. These simulation findings are consistent with the experimental observations of the de-aggregation of **1** and **2** in 70% *n*-hexane-$CHCl_3$ upon addition of $C_5F_{11}COOH$.

We have further characterized the pairwise interactions between **3** and various solvent components through analysis of RDF $g_{Pt-solvent}(r)$ curves. The $g_{Pt-solvent}(r)$ profile for **3** in the 70% *n*-hexane-$CHCl_3$ mixture (Fig. 4b) demonstrates that $CHCl_3$ molecules can approach the Pt(II) center closely, forming multiple solvation shells around **3**. On the other hand, no such solvation shell is observed between **3** and *n*-hexane molecules. These results indicate that *n*-hexane molecules promote the aggregation of **3** into higher-order structures, whereas in $CHCl_3$, **3** primarily exists as monomers or lower-order aggregates. Interestingly, $C_6F_{13}Br$ behaves similarly to *n*-hexane in its interaction with **3**, as revealed in the $g_{Pt-C_6F_{13}Br}(r)$ profile (Fig. 4c). In contrast, $C_5F_{11}COOH$ and $C_5H_{11}COOH$ exhibit strong affinity toward **3**, facilitating the formation of more robust solvation shells than those observed with $CHCl_3$. The strong interactions between $C_5F_{11}COOH$ and **3** could compete with the Pt(II)$\cdots$Pt(II) and π–π stacking interactions between the complex cations. This competition is likely concentration-dependent, and the de-aggregation of **3** might occur at a suitable $C_5F_{11}COOH$ concentration. However, despite the high affinity of $C_5H_{11}COOH$ toward **3**, it does not promote the de-aggregation of **3**, as revealed by both experimental and computational (Fig. 4a) observations. The interactions between the acid molecules with major solvent components (*n*-hexane and $CHCl_3$) have also been investigated *via* RDF $g_{acid-solvent}(r)$. While both acid molecules exhibit comparable pairwise interaction profiles with $CHCl_3$ molecules (Fig. 4d), $C_5F_{11}COOH$ molecules clearly form stronger interactions with *n*-hexane molecules, as indicated by the first *n*-hexane solvation shell at approximately $r = 0.7$ nm (Fig. 4e).

Given the predominance of *n*-hexane within the mixed solvent system employed in the experiments, we have proposed a hypothesis to rationalize the distinct supramolecular self-assembly behavior of **1** and **2** in the presence of $C_5F_{11}COOH$ and $C_5H_{11}COOH$ (Fig. S24) based on the simulation results of **3**. The presence of $C_5F_{11}COOH$ molecules in 70% *n*-hexane-$CHCl_3$ maximizes its contact surface area for interactions with surrounding *n*-hexane solvent molecules and with **1** or **2**. These interactions result in the de-aggregation of **1** or **2** into monomers or lower-order aggregates. Conversely, $C_5H_{11}COOH$ minimizes the contact surface area with the surrounding *n*-hexane solvent molecules while interacting with **1** or **2**. The weaker affinity of $C_5H_{11}COOH$ toward *n*-hexane allows **1** or **2** to retain in relatively higher-order aggregates. Consistent results could be obtained from the replicated simulations with different initial configurations (Fig. S25).

Motivated by the pronounced spectral responses, attempts have been made to employ the liquid-phase extraction method to detect and extract PFASs in water using **1** and **2** as a proof of concept. Upon the addition of PFHxA, PFBA, TFA or controls separately to deionized water, followed by vigorous shaking with the organic phase containing **1** or **2** (volume ratio of organic phase : aqueous phase = 1 : 1), only PFHxA triggers an almost immediate PL color shift in the organic layer (Fig. 5a, b and S26). $^{19}F\{H\}$ NMR spectra (Fig. S27 and S28) of the organic phase after extraction suggest efficient extraction of PFHxA from the aqueous phase. The substantial differences in luminescence enhancement observed among PFHxA, PFBA, and TFA can be attributed to the stronger interaction of PFHxA with Pt(II) complexes and its more hydrophobic nature, owing to its more extensive perfluoroalkyl chain, which facilitates its partitioning into the organic phase. The PL color shift in the organic layer indicates subsequent de-aggregation of **1** and **2**. With an equivalent concentration of PFHxA in the aqueous phase and a comparable concentration of platinum(II) complex in the organic phase, it is found that **2** induces a more significant PL intensity change than **1** (Fig. S29 and S30). The investigation has been further extended to comparison studies with other related PFASs, including PFOA, perfluorobutanesulfonic acid (PFBS), and perfluorohexanesulfonic acid (PFHxS). The results show that PFHxA induces a more pronounced blue shift of the emission of the organic phase than PFHxS and PFBS (Fig. S31a), implying that PFHxA promotes a greater extent of de-aggregation, as evidenced by the monomeric emission at 540 nm. Nonetheless, similar emission spectral changes are observed when PFOA is extracted into the organic phase. The similar spectroscopic response towards PFHxA and PFOA is likely attributable to their comparable interactions with **2** and the surrounding solvent molecules. We have also demonstrated that the extraction and detection of PFBA can be achieved by adding NaCl or KCl into the aqueous medium (Fig. S32–S34). This process increases the ionic strength in the aqueous phase, thereby enhancing the extraction efficiency of PFBA into the organic phase. Moreover, the original orange-red ^{3}MMLCT emission of **2** in the organic phase can be restored by neutralizing the acidity with NEt_3 or Na_2CO_3 (Fig. S35 and S36), enabling **2** to undergo re-assembly and to be reused for PFHxA detection over multiple cycles (Fig. S37). More importantly, control extractions with dilute HNO_3 ($pK_a = -1.4$)[62] or sodium perfluorohexanoate (NaPFHx) show no PL changes (Fig. S38) similar to those demonstrated in PFHxA ($pK_a = -0.16$)[63] and PFBA ($pK_a = 0.08$).[64] These findings suggest that both the anionic fluorinated alkyl chain and the solvated H^+ are essential for PFAS detection with platinum(II) complexes using the liquid-phase extraction approach.

The responsiveness of **2** in the liquid-phase extraction of PFHxA is assessed by varying the initial concentration of PFHxA in the aqueous phase and monitoring the PL changes (Fig. 5c and S39). The relative emission intensity at 550 nm demonstrates a sigmoidal relationship with the concentration of PFHxA in the aqueous phase (Fig. 5c and S39). It has been observed that reducing the concentration of **2** in the organic phase does not influence the response to PFHxA (Fig. S40a). When a 2 M NaCl solution is employed as the aqueous phase, the dynamic range[65] is reduced from 8.7–106.3 mM to 10.4–42.0 mM. According to the equation $y_{LOD} = y_{Blank} + 3\sigma_{Blank}$, where y_{LOD} is the LOD of the sensor, y_{Blank} is the average of the blank

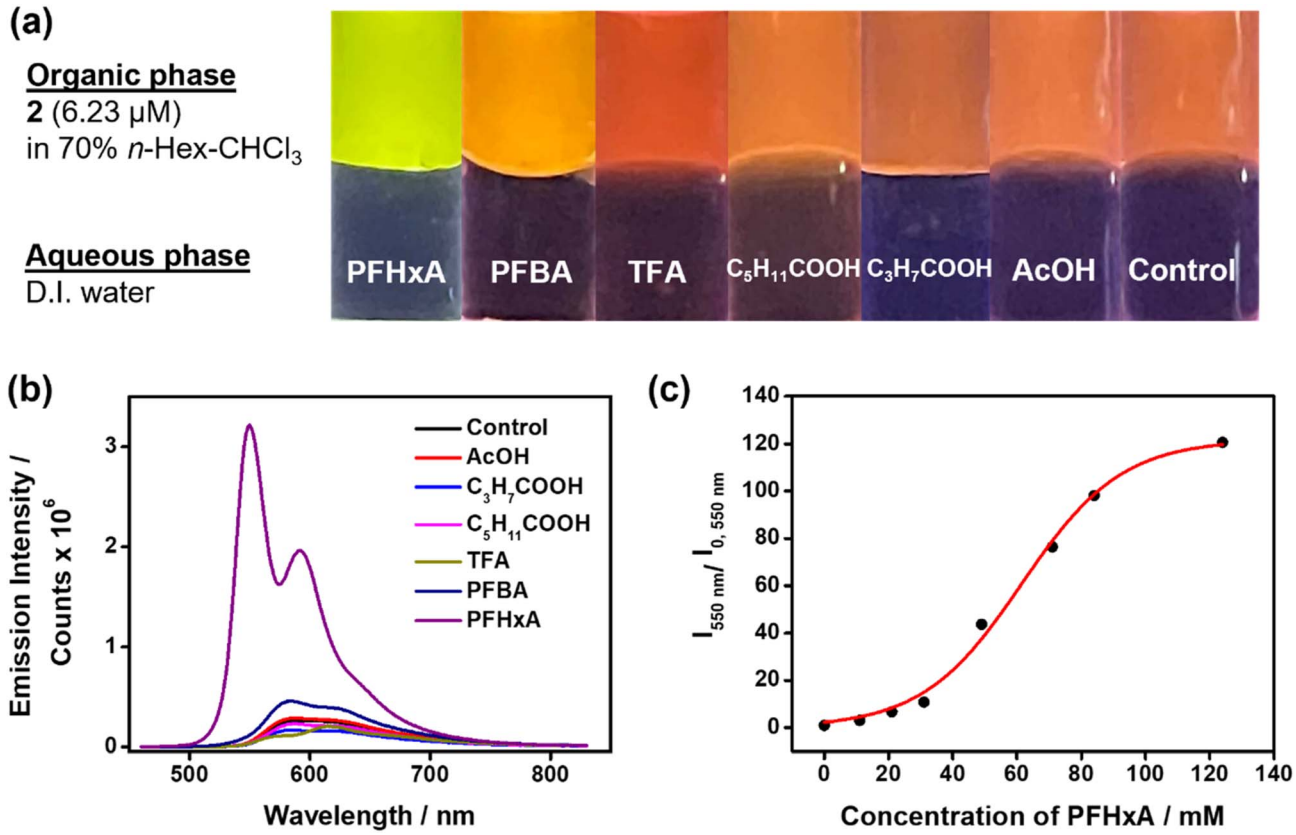

Fig. 5 (a) Photographs under a UV-light source (λ_{ex} = 365 nm) and (b) emission spectra of **2** in 70% *n*-hexane-$CHCl_3$ (6.23 μM, 2 mL) after extraction with various species in deionized water (125 mM, 2 mL). The excitation wavelength is 425 nm. (c) A plot of relative emission intensity at 550 nm against initial concentration of PFHxA in the aqueous phase.

sample and σ_{Blank} is the standard deviation of the blank sample,[65] it is found that the limit of detection (LOD) for PFHxA is 9.41 mM (Fig. S40b).

Conclusion

In conclusion, we have designed and synthesized multinuclear platinum(II) complexes capable of self-assembling into 2D SPs. In *n*-hexane-$CHCl_3$ solution mixture, the self-assembly behavior of the platinum(II) complexes can be modulated upon exposure to acidic PFASs, generating pronounced absorbance changes and naked-eye visible photoluminescence color shifts. By leveraging the liquid-phase extraction method, we have demonstrated the reversible detection and uptake of PFHxA in deionized water. This study highlights the innovative use of platinum(II) complexes for proof-of-concept detection and extraction of PFHxA in deionized water, and provides a fundamental understanding of the underlying mechanism with the support of MD simulations. Although the current system cannot be employed for the immediate practical application of PFHxA detection, this study is expected to provide important insights into the use of simple building blocks for the development of sophisticated assemblies with functional properties. Future work will focus on the development of such 2D porous SPs that can be readily disassembled and re-assembled for on-demand detection and extraction.

Author contributions

Vivian W.-W. Yam initiated and designed the research. Vivian W.-W. Yam, Zhen Chen, Eric K.-H. Wong and Nicholas C.-M. Yeung designed and synthesized the platinum(II) complexes. Nicholas C.-M. Yeung conducted characterization, photophysical measurements and morphological studies. Nicholas C.-M. Yeung and Zhen Chen conducted supramolecular assembly studies with PFASs. Ziyong Chen conducted computational studies. Vivian W.-W. Yam, Nicholas C.-M. Yeung, Zhen Chen and Eric K.-H. Wong wrote the manuscript. Vivian W.-W. Yam and Zhen Chen supervised the work. All authors analyzed the data, discussed the results and contributed to the final manuscript.

Conflicts of interest

There are no conflicts to declare.

Data availability

Supplementary information (SI): further details on experimental procedures, computational details, UV-vis absorption and emission spectra, NMR spectra, DLS traces, WAXS and GI-XRD data. See DOI: https://doi.org/10.1039/d6sc00989a.

Acknowledgements

Vivian W.-W. Yam acknowledges financial support from the General Research Fund (HKU 17311224) of the Research Grants Council of the Hong Kong Special Administrative Region, People's Republic of China. Support from the Innovation Technology Commission to the State Key Laboratory of Synthetic Chemistry is acknowledged. Nicholas C.-M. Yeung acknowledges the receipt of postgraduate studentships administered by The University of Hong Kong. We also thank the Large Research Equipment Fund (LREF) Scheme for Facilities for Advanced Structural Characterization and Structural Dynamics for Self-Assembling Systems and Soft Materials Beyond the Molecular Level. The Electron Microscope Unit of the University of Hong Kong and the Testing Technology Center of Materials and Devices of Tsinghua Shenzhen International Graduate School (Tsinghua SIGS) are acknowledged for providing technical assistance with SEM and AFM experiments. Mr Liu Li is acknowledged for his assistance with SEM measurements in Tsinghua SIGS. The computations were performed using research computing facilities offered by the Information Technology Services at The University of Hong Kong.

References

1 E. L. Schymanski, J. Zhang, P. A. Thiessen, P. Chirsir, T. Kondic and E. E. Bolton, Per- and Polyfluoroalkyl Substances (PFAS) in PubChem: 7 Million and Growing, *Environ. Sci. Technol.*, 2023, **57**, 16918–16928.

2 PFAS Explained. https://www.epa.gov/pfas/pfas-explained, accessed February 2026.

3 Our Current Understanding of the Human Health and Environmental Risks of PFAS. https://www.epa.gov/pfas/our-current-understanding-human-health-and-environmental-risks-pfas, accessed February 2026.

4 R. C. Buck, J. Franklin, U. Berger, J. M. Conder, I. T. Cousins, P. de Voogt, A. A. Jensen, K. Kannan, S. A. Mabury and S. P. van Leeuwen, Perfluoroalkyl and Polyfluoroalkyl Substances in the Environment: Terminology, Classification, and Origins, *IEAM*, 2011, **7**, 513–541.

5 G. Munoz, H. Budzinski, M. Babut, H. Drouineau, M. Lauzent, K. L. Menach, J. Lobry, J. Selleslagh, C. Simonnet-Laprade and P. Labadie, Evidence for the Trophic Transfer of Perfluoroalkylated Substances in a Temperate Macrotidal Estuary, *Environ. Sci. Technol.*, 2017, **51**, 8450–8459.

6 S. Zahm, J. P. Bonde, W. A. Chiu, J. Hoppin, J. Kanno, M. Abdallah, C. R. Blystone, M. M. Calkins, G.-H. Dong, D. C. Dorman, *et al.*, Carcinogenicity of Perfluorooctanoic Acid and Perfluorooctanesulfonic Acid, *Lancet Oncol.*, 2024, **25**, 16–17.

7 Per- and Polyfluoroalkyl Substances (PFAS) - Final PFAS National Primary Drinking Water Regulation. https://www.epa.gov/sdwa/and-polyfluoroalkyl-substances-pfas, accessed February 2026.

8 Amending Annex XVII to Regulation (EC) No 1907/2006 of the European Parliament and of the Council as Regards Undecafluorohexanoic Acid (PFHxA), Its Salts and PFHxA-related Substances, https://eur-lex.europa.eu/legal-content/EN/TXT/HTML/?uri=PI_COM:C(2024)5277, accessed February 2026.

9 Y.-D. Yang, Q. Zhang, X. Jin, C. V. Chau, J. Yang, G. Henkelman, X. Chi, H.-Y. Gong, R. J. Hooley and J. L. Sessler, Readily Visualized Perfluorooctanoic Acid Detection Using a Small Molecule Chemosensor, *Angew. Chem., Int. Ed.*, 2025, **64**, e202501245.

10 R. Dalapati, S. Manickam, J. Shi, M. Hunter and L. Zang, Perylene Diimide Based Fluorescent Sensors for Aqueous Detection of Perfluorooctane Sulfonate (PFOS), *Anal. Chim. Acta*, 2025, **1341**, 343670.

11 X. Zhu, C. Cheng, X. Qin and Y. Wang, β-Cyclodextrin Imprinted Film Embedded with Methylene Blue: A Host-guest Sensitive Electrochemical Strategy for PFAS Detection, *J. Hazard. Mater.*, 2025, **485**, 136870.

12 Z. Zheng, H. Yu, W.-C. Geng, X.-Y. Hu, Y.-Y. Wang, Z. Li, Y. Wang and D.-S. Guo, Guanidinocalix[5]arene for Sensitive Fluorescence Detection and Magnetic Removal of Perfluorinated Pollutants, *Nat. Commun.*, 2019, **10**, 5762.

13 E. E. Harrison and M. L. Waters, Detection and Differentiation of Per- and Polyfluoroalkyl Substances (PFAS) in Water Using a Fluorescent Imprint-and-Report Sensor Array, *Chem. Sci.*, 2023, **14**, 928–936.

14 H. Niu, S. Wang, Z. Zhou, Y. Ma, X. Ma and Y. Cai, Sensitive Colorimetric Visualization of Perfluorinated Compounds Using Poly(ethylene glycol) and Perfluorinated Thiols Modified Gold Nanoparticles, *Anal. Chem.*, 2014, **86**, 4170–4177.

15 A. Concellón, J. Castro-Esteban and T. M. Swager, Ultratrace PFAS Detection Using Amplifying Fluorescent Polymers, *J. Am. Chem. Soc.*, 2023, **145**, 11420–11430.

16 H. Liu, Q.-f. Xu, Z.-z. Zhang, Y.-n. Li and C.-y. Zhang, A Fluorescent Conjugated Polymer-based Ratiometric Aptasensor for Highly Specific and Robust Detection of Perfluorooctanoic acid, *Chem. Commun.*, 2026, **62**, 3531–3535.

17 M. H. Hassan, R. Khan, D. Andreescu, S. Shrestha, M. Cotlet and S. Andreescu, Atomically Precise Hexanuclear Ce(IV) Clusters as Functional Fluorescent Nanosensors for Rapid One-Step Detection of PFAS, *Adv. Funct. Mater.*, 2024, **34**, 2403364.

18 R. Dalapati, M. Hunter, M. Sk, X. Yang and L. Zang, Fluorescence Turn-on Detection of Perfluorooctanoic Acid (PFOA) by Perylene Diimide-Based Metal–Organic Framework, *ACS Appl. Mater. Interfaces*, 2024, **16**, 32344–32356.

19 R. Dalapati, J. Shi, M. Hunter and L. Zang, Dual-functional Metal–organic Framework for Efficient Removal and Fluorescent Detection of Perfluorooctanoic Acid (PFOA) From Water, *J. Mater. Chem. C*, 2025, **13**, 16753–16762.

20 D. M. Roundhill, H. B. Gray and C. M. Che, Pyrophosphito-Bridged Diplatinum Chemistry, *Acc. Chem. Res.*, 1989, **22**, 55–61.

21 V. H. Houlding and V. M. Miskowski, The Effect of Linear Chain Structure on the Electronic Structure of Pt(II) Diimine Complexes, *Coord. Chem. Rev.*, 1991, **111**, 145–152.
22 J. A. Bailey, V. M. Miskowski and H. B. Gray, Spectroscopic and Structural properties of Binuclear Platinum-terpyridine Complexes, *Inorg. Chem.*, 1993, **32**, 369–370.
23 K. M.-C. Wong; V. K.-M. Au and V. W.-W. Yam, 8.03-Noncovalent Metal-metal Interactions, in *Comprehensive Inorganic Chemistry II*, ed. Reedijk, J. and Poeppelmeier, K., Elsevier, Oxford, U.K., 2013, 2nd ed, pp. 59–130.
24 V. W.-W. Yam and A. S.-Y. Law, Luminescent d^8 Metal Complexes of Platinum(II) and Gold(III): From Photophysics to Photofunctional Materials and Probes, *Coord. Chem. Rev.*, 2020, **414**, 213298.
25 K. M.-C. Wong and V. W.-W. Yam, Self-Assembly of Luminescent Alkynylplatinum(II) Terpyridyl Complexes: Modulation of Photophysical Properties through Aggregation Behavior, *Acc. Chem. Res.*, 2011, **44**, 424–434.
26 V. W.-W. Yam, V. K.-M. Au and S. Y.-L. Leung, Light-Emitting Self-Assembled Materials Based on d^8 and d^{10} Transition Metal Complexes, *Chem. Rev.*, 2015, **115**, 7589–7728.
27 Y. Han, Z. Gao, C. Wang, R. Zhong and F. Wang, Recent Progress on Supramolecular Assembly of Organoplatinum(II) Complexes into Long-range Ordered Nanostructures, *Coord. Chem. Rev.*, 2020, **414**, 213300.
28 A. Aliprandi, M. Mauro and L. De Cola, Controlling and Imaging Biomimetic Self-assembly, *Nat. Chem.*, 2016, **8**, 10–15.
29 Z. Chen, A. K.-W. Chan, V. C.-H. Wong and V. W.-W. Yam, A Supramolecular Strategy toward an Efficient and Selective Capture of Platinum(II) Complexes, *J. Am. Chem. Soc.*, 2019, **141**, 11204–11211.
30 Z. Chen and V. W.-W. Yam, Precise Size-Selective Sieving of Nanoparticles Using a Highly Oriented Two-Dimensional Supramolecular Polymer, *Angew. Chem., Int. Ed.*, 2020, **59**, 4840–4845.
31 Z. Chen, M. H.-Y. Chan and V. W.-W. Yam, Stimuli-Responsive Two-Dimensional Supramolecular Polymers Based on Trinuclear Platinum(II) Scaffolds: Reversible Modulation of Photoluminescence, Cavity Size, and Water Permeability, *J. Am. Chem. Soc.*, 2020, **142**, 16471–16478.
32 S. Y.-L. Leung, K. M.-C. Wong and V. W.-W. Yam, Self-assembly of Alkynylplatinum(II) Terpyridine Amphiphiles into Nanostructures *via* Steric Control and Metal–metal Interactions, *Proc. Natl. Acad. Sci. U. S. A.*, 2016, **113**, 2845–2850.
33 J. K.-L. Poon, Z. Chen, S. Y.-L. Leung, M.-Y. Leung and V. W.-W. Yam, Geometrical Manipulation of Complex Supramolecular Tessellations by Hierarchical Assembly of Amphiphilic Platinum(II) Complexes, *Proc. Natl. Acad. Sci. U. S. A.*, 2021, **118**, e2022829118.
34 H.-Z. Wang, M. H.-Y. Chan, Z. Chen, Z.-Y. Chen, M.-Y. Leung and V. W.-W. Yam, Supramolecular Self-assembly of Dinuclear Alkynylplatinum(II) Complexes into Highly-ordered Crystalline Hexagonal Bipyramid Superstructures, *Chem*, 2023, **9**, 3573–3587.
35 X. Hao, B. Xiong, M. Ni, B. Tang, Y. Ma, H. Peng, X. Zhou, I. I. Smalyukh and X. Xie, Highly Luminescent Liquid Crystals in Aggregation Based on Platinum(II) Complexes, *ACS Appl. Mater. Interfaces*, 2020, **12**, 53058–53066.
36 C. A. Strassert, C.-H. Chien, M. D. Galvez Lopez, D. Kourkoulos, D. Hertel, K. Meerholz and L. De Cola, Switching On Luminescence by the Self-Assembly of a Platinum(II) Complex into Gelating Nanofibers and Electroluminescent Films, *Angew. Chem., Int. Ed.*, 2011, **50**, 946–950.
37 A. Y.-Y. Tam, K. M.-C. Wong, G. Wang and V. W.-W. Yam, Luminescent Metallogels of Platinum(II) Terpyridyl Complexes: Interplay of Metal···Metal, π–π and Hydrophobic–Hydrophobic Interactions on Gel Formation, *Chem. Commun.*, 2007, 2028–2030.
38 A. Y.-Y. Tam, K. M.-C. Wong and V. W.-W. Yam, Unusual Luminescence Enhancement of Metallogels of Alkynylplatinum(II) 2,6-Bis(*N*-alkylbenzimidazol-2′-yl) pyridine Complexes upon a Gel-to-Sol Phase Transition at Elevated Temperatures, *J. Am. Chem. Soc.*, 2009, **131**, 6253–6260.
39 M. H.-Y. Chan, M. Ng, S. Y.-L. Leung, W. H. Lam and V. W.-W. Yam, Synthesis of Luminescent Platinum(II) 2,6-Bis(*N*-dodecylbenzimidazol-2′-yl)pyridine Foldamers and Their Supramolecular Assembly and Metallogel Formation, *J. Am. Chem. Soc.*, 2017, **139**, 8639–8645.
40 Y. Zhang, Q.-F. Zhou, G.-F. Huo, G.-Q. Yin, X.-L. Zhao, B. Jiang, H. Tan, X. Li and H.-B. Yang, Hierarchical Self-Assembly of an Alkynylplatinum(ll) Bzimpy-Functionalized Metallacage *via* Pt···Pt and π–π Interactions, *Inorg. Chem.*, 2018, **57**, 3516–3520.
41 A. K.-W. Chan and V. W.-W. Yam, Precise Modulation of Molecular Building Blocks from Tweezers to Rectangles for Recognition and Stimuli-Responsive Processes, *Acc. Chem. Res.*, 2018, **51**, 3041–3051.
42 J. Y.-W. Yeung, F. K.-W. Kong, F. K.-W. Hau, M. H.-Y. Chan, M. Ng, M.-Y. Leung and V. W.-W. Yam, Solvent-Dependent Supramolecular Host–Guest Assemblies of Platinum(II) Tweezers and a Guest System: From Discrete Molecules to High-Ordered Oligomers, *Angew. Chem., Int. Ed.*, 2022, **61**, e202207313.
43 Y. Xu, M.-Y. Leung, L. Yan, Z. Chen, P. Li, Y.-H. Cheng, M. H.-Y. Chan and V. W.-W. Yam, Synthesis, Characterization, and Resistive Memory Behaviors of Highly Strained Cyclometalated Platinum(II) Nanohoops, *J. Am. Chem. Soc.*, 2024, **146**, 13226–13235.
44 W. C. Poh, H.-L. Au-Yeung, A. K.-W. Chan, E. Y.-H. Hong, Y.-H. Cheng, M.-Y. Leung, S.-L. Lai, K.-H. Low and V. W.-W. Yam, Cyclometalated Platinum(II) Complexes with Donor-Acceptor-Containing Bidentate Ligands and Their Application Studies as Organic Resistive Memories, *Chem.–Asian J.*, 2021, **16**, 3669–3676.
45 A. S.-H. Cheung, E. Y.-H. Hong and V. W.-W. Yam, Phosphole Oxide-based Cyclometalated Platinum(II) β-Diketonate Complexes for Cooperative Self-assembly and Solution-processable Resistive Memories with Excellent Stability, *Inorg. Chem. Front.*, 2025, **12**, 3873–3885.

46 J. Guo, E. K.-H. Wong, G.-X. Xu, A. S.-Y. Law, M. H.-Y. Chan, J. Lam, Z. Chen, K. K.-W. Lo and V. W.-W. Yam, Self-Assembly of Alkynylplatinum(II) Complexes for Sialic Acid Detection and Differentiation of Cancer Cells from Normal Cells, *J. Am. Chem. Soc.*, 2025, **147**, 21629–21637.

47 A. L.-Y. So, J. Guo, H. Yuan, Q. Shen, E. K.-H. Wong, S. Wang and V. W.-W. Yam, Ensembles of Cationic Conjugated Polymer and Anionic Platinum(II) Complexes: From FRET Properties to Application Studies in E. coli Imaging and Singlet Oxygen Generation, *Chem. Sci.*, 2025, 13684–13693.

48 T. Rex, T. Mößer, R. R. C. Vilela, A. Hepp, C. Grashoff and C. A. Strassert, Supramolecular Assembly of Water-Soluble Platinum(II) Complexes: From Emission Modulation to Cell Imaging in Specific Organelles, *Chem.–Eur. J.*, 2025, **31**, e202404432.

49 Y. Wang, N. Li, L. Chu, Z. Hao, J. Chen, J. Huang, J. Yan, H. Bian, P. Duan, J. Liu, *et al.*, Dual Enhancement of Phosphorescence and Circularly Polarized Luminescence through Entropically Driven Self-Assembly of a Platinum(II) Complex, *Angew. Chem., Int. Ed.*, 2024, **63**, e202403898.

50 Z. Shu, Y. Zhang, Z. Ni, G. Xiao, Z. Chi, Y. Li and Y. Ai, Unusual Optical Switches of Platinum(II) Foldamers for Stepwise Photonic Information Storage Materials, *Adv. Opt. Mater.*, 2025, **13**, 2500065.

51 J. P. Byrne, J. A. Kitchen and T. Gunnlaugsson, The btp [2,6-bis(1,2,3-triazol-4-yl)pyridine] Binding Motif: A New Versatile Terdentate Ligand for Supramolecular and Coordination Chemistry, *Chem. Soc. Rev.*, 2014, **43**, 5302–5325.

52 K. Sonogashira, Development of Pd–Cu Catalyzed Cross-Coupling of Terminal Acetylenes with sp^2-Carbon Halides, *J. Organomet. Chem.*, 2002, **653**, 46–49.

53 Y. Li, L. Zhao, A. Y.-Y. Tam, K. M.-C. Wong, L. Wu and V. W.-W. Yam, Luminescent Amphiphilic 2,6-Bis(1,2,3-triazol-4-yl)pyridine Platinum(II) Complexes: Synthesis, Characterization, Electrochemical, Photophysical, and Langmuir–Blodgett Film-Formation Studies, *Chem.–Eur. J.*, 2013, **19**, 14496–14505.

54 Y. Li, L. Chen, Y. Ai, E. Y.-H. Hong, A. K.-W. Chan and V. W.-W. Yam, Supramolecular Self-Assembly and Dual-Switch Vapochromic, Vapoluminescent, and Resistive Memory Behaviors of Amphiphilic Platinum(II) Complexes, *J. Am. Chem. Soc.*, 2017, **139**, 13858–13866.

55 H. DeVoe, The Theory of Hypochromism of Biopolymers: Calculated Spectra for DNA, *Ann. N. Y. Acad. Sci.*, 1969, **158**, 298–307.

56 T. Lu and F. Chen, A Multifunctional Wavefunction Analyzer, *J. Comput. Chem.*, 2012, **33**, 580–592.

57 J. Wang, R. M. Wolf, J. W. Caldwell, P. A. Kollman and D. A. Case, Development and Testing of a General Amber Force Field, *J. Comput. Chem.*, 2004, **25**, 1157–1174.

58 D. Van Der Spoel, E. Lindahl, B. Hess, G. Groenhof, A. E. Mark and H. J. C. Berendsen, GROMACS: Fast, Flexible, and Free, *J. Comput. Chem.*, 2005, **26**, 1701–1718.

59 *Sobtop, Version 1.0 (dev5)*. https://sobereva.com/soft/Sobtop, accessed November, 2025.

60 X. Zheng, M. H.-Y. Chan, A. K.-W. Chan, S. Cao, M. Ng, F. K. Sheong, C. Li, E. C. Goonetilleke, W. W. Y. Lam, T.-C. Lau, *et al.*, Elucidation of the Key Role of Pt···Pt Interactions in the Directional Self-assembly of Platinum(II) Complexes, *Proc. Natl. Acad. Sci. U. S. A.*, 2022, **119**, e2116543119.

61 T. H.-Y. Chan, Z. Chen, M.-Y. Leung, M. H.-Y. Chan, E. K.-H. Wong, W. K. Tang and V. W.-W. Yam, Thermoresponsive Platinum(II) 2,6-Di(pyrid-2-yl)pyrazine Complexes with Unusual Aggregation Behavior upon Heating, *J. Am. Chem. Soc.*, 2025, **147**, 24941–24949.

62 R. P. Bell, *The Proton in Chemistry*, Cornell University Press, 1973, 2nd edn.

63 M. M. Angrish, L. Dishaw, J. A. Davis, J. L. Dean II, A. Kraft, E. G. Radke, P. Schlosser, Y.-S. Lin, S. White and J. Zhao, *et al.*, *IRIS Toxicological Review of Perfluorohexanoic Acid [PFHxA, CASRN 307-24-4] and Related Salts; EPA/635/R-23/027Fa; Center for Public Health and Environmental Assessment, Office of Research and Development*, U.S. Environmental Protection Agency, Washington, DC, 2023, https://iris.epa.gov/static/pdfs/0704tr.pdf.

64 J. A. Davis, M. M. Taylor, A. Kraft, J. C. Lambert, E. Radke and P. Schlosser, *IRIS Toxicological Review of Perfluorobutanoic Acid (PFBA, CASRN 375-22-4) and Related Salts; EPA/635/R-22/277Fa; Center for Public Health and Environmental Assessment, Office of Research and Development*, U.S. Environmental Protection Agency, Washington, DC, 2022, https://cfpub.epa.gov/ncea/iris/iris_documents/documents/toxreviews/0701tr.pdf.

65 N. De Acha, A. B. Socorro-Leránoz, C. Elosúa and I. R. Matías, Trends in the Design of Intensity-Based Optical Fiber Biosensors (2010–2020), in *Biosensors*, 2021, vol. 11, p. 197.